Science Arts & Métiers (SAM)
is an open access repository that collects the work of Arts et Métiers Institute of Technology researchers and makes it freely available over the web where possible.

This is an author-deposited version published in: https://sam.ensam.eu
Handle ID: .http://hdl.handle.net/10985/14636

To cite this version :

Mohamed Besher BARADI, Camilo CRUZ, Thomas RIEDEL, Gilles REGNIER - Mechanical and microstructural characterization of flowing weld lines in injection-molded short fiber-reinforced PBT - Polymer Testing - Vol. 74, p.152-162 - 2019

Any correspondence concerning this service should be sent to the repository Administrator : scienceouverte@ensam.eu

Material Properties

Mechanical and microstructural characterization of flowing weld lines in injection-molded short fiber-reinforced PBT

Mohamed Besher Baradi[a,b], Camilo Cruz[b], Thomas Riedel[c], Gilles Régnier[a,*]

[a] PIMM, Arts et Métiers ParisTech, CNRS, CNAM, France
[b] Robert Bosch GmbH, Corporate Sector Research and Advance Engineering, Plastics Engineering, 71272, Renningen, Germany
[c] Robert Bosch GmbH, Corporate Sector Research and Advance Engineering, Analytics, 71272, Renningen, Germany

ARTICLE INFO

Keywords:
Weld lines
Short-fiber composites
Mechanical properties
Non-destructive testing
Injection molding
Digital image correlation

ABSTRACT

The aim of this work is an extensive experimental mechanical and microstructural characterization of flowing weld lines (WLs) in injection-molded short glass fiber-reinforced polybutylenterephthalate (PBT) using X-ray computed tomography and digital image correlation (DIC). It was found that the induced fiber orientation (FO) in a flowing WL is similar to that induced by flow along a wall. In this test case, the impact of the flowing WL on the FO did not vanish after a flow length of 70 mm. The shape of the inserts, which originated the flowing WLs, only had a marginal effect on the induced FO gradient. By reducing part thickness, the erasing of the FO gradient induced by the WL is reached at shorter flow distances. At the WLs, there is a reduction of the fiber volume fraction in comparison to the regions far from the WL plane. DIC results show a pronounced strain localization at the WL, which can be explained by the FO gradient induced by the WL.

1. Introduction

In injection-molded thermoplastic parts, weld lines (WLs) form during the filling phase at the interface where two melt fronts collide. Multiple injection gates, inserts or pins inside the mold cavity lead to the separation of the melt and WL formation. WLs induce a significant reduction of the mechanical properties, especially in the case of short fiber-reinforced polymers. The occurrence of WLs is nearly unavoidable in complex industrial parts and they often cause the failure of those parts [1]. Current industrial and environmental needs demand a reliable prediction of the mechanical properties at the WLs for an improved economical design. This requires comprehensive physical and mechanical understanding of the process-induced microstructure at the WLs. The effect of WLs on the mechanical properties of fiber-reinforced thermoplastics has been studied extensively [1–11,14–16].

Most of the research on WLs shows mechanical characterizations considering the influence of process parameters, filler content and angle of WL formation. According to literature, the WL strength is improved slightly by setting higher melt temperatures [7,10]. It has been shown that the severity of a WL increases with the filler content [8]. On the other hand, some authors reported an increase of WL strength by enlarging the insert size for flowing WLs made of unreinforced polystyrene [10]. The weakness of a WL can be attributed to the following phenomena [1–9]:

1 **Incomplete molecular diffusion (insufficient healing of the polymer matrix)**: Due to the rapid cooling rates in injection molding, the polymer chains might have less time than required to reptate and reach the entanglement density of the bulk.
2 **Strong fiber orientation (FO) gradient**: Fibers align parallel to the WL surface, substantially reducing their role in strengthening the part across the WL plane.
3 **High molecular orientation:** Because of the fountain flow phenomenon, the molecules also orient parallel to the WL surface. The molecular orientation however has a negligible contribution to the strength reduction in comparison with the FO gradient [11].
4 **V-notches:** The formation of V-notches at the surface of WLs has been documented elsewhere [1,6]. They act as stress concentrators at the WLs, but their formation can be avoided by using ventilation channels and controlling the process parameters, especially the packing (holding) pressure.

Investigations of the microstructure near the WLs and its influence on the mechanical properties is less common in the literature. In this work, the focus is put on the microstructural aspect of WLs. Vaxman et al. [12] used reflected light microscopy to show that in a frontal WL the fibers tend to align parallel to the WL surface. Other researchers used scanning electron microscopy for studying the FO at the WLs [9] and found that the fibers in flowing WLs orient in the flow direction

* Corresponding author. Arts et Métiers ParisTech – PIMM, 151 bd de l'Hôpital, 75013, Paris, France.
E-mail address: gilles.regnier@ensam.eu (G. Régnier).

through the thickness, eliminating the typical skin-core microstructure.

The use of X-ray computed tomography (CT) enables a three-dimensional reconstruction of the microstructure of fiber-reinforced thermoplastics. Prade el al. [13] used X-ray vector radiography on fiber-reinforced parts with flowing WLs to validate the characterization method. The authors showed a qualitative assessment of the FO at the WL, but the detailed microstructure of the WL does not appear in their publication. In other work [14], based on several CT scans at different positions along a flowing WL, an increase of FO in the out-of-plane direction at the core of the WL was reported. Another group used X-ray scatter dark field imaging and X-ray CT to describe the FO at a flowing WL [15]. They confirmed that in a flowing WL the main FO direction is parallel to the flow. Microstructural analysis with X-ray CT at a flowing WL by Ayadi et al. [16] showed a complex FO across the thickness after the insert. The authors noticed a FO gradient around the WL and random FO at the weld region. The higher strain localization at the WL was attributed to the existence of out-of-plane fibers at the core layer of the WL zone. Using a larger scale analysis at the WL, Ayadi et al. [17] arrived to the same conclusion. In addition, they analyzed the FO and fiber volume fraction (VF) quantitatively, showing changes both in WL direction and transversally to the WL plane. According to the publication, the variations in VF are also responsible for the variations of the mechanical properties.

Yamada et al. [6] showed that in a flowing WL (made of an unreinforced thermoplastic) the mechanical behavior is highly influenced by the molecular morphology at the surface of the WL. The main factor reducing the mechanical properties at the WL was the V-notch, which induced a stress concentration over the polymer layer beneath it, which was not completely healed. Furthermore, they noticed a high molecular orientation in the flow direction at the WL. The use of DIC to study the strain field during the tensile test of a bar containing a flowing WL was reported by Kalus et al. [19]. They showed the development of a strong strain localization at the WL. In the case of a 30 wt% glass fiber-reinforced PA12, the strain was localized in a region of 2 mm around the WL. Based on the convergence of the estimated local elastic modulus at the WL for the fiber-reinforced and unreinforced PA12 tensile bars, they suggested that there is no fiber crossing at the WL in the fiber-reinforced case.

In general, the available characterizations of the microstructure at WLs are mainly qualitative and limited to relative small regions around the WL. In this work, a specific mold to perform a comprehensive microstructural study of flowing WLs was developed. Firstly stresses and strains at break were measured to mechanically quantify the effect of WLs. Both FO and VF at different positions along the WL were quantified by analyzing X-ray computed tomography data. The effect of the insert shape and part thickness on the induced FO gradients was studied. The plate thickness changes at the WL were also measured in order to correlate it with the induced FO. The induced FO and the mechanical tensile tests results were analyzed in front of the strain fields measured with digital image correlation (DIC).

2. Experimental methods

2.1. Sample preparation

A polybutylene-terephthalate reinforced with 30 wt% glass fibers (average VF of 0.18) was used. The glass fibers in the composite had a mean fiber length of 200 μm, a diameter of 10 μm and cylindrical shape. The flowing WL mold was designed with the assistance of rheological simulations using Moldflow® 2016. It was found that the bigger the insert the greater the influence on the FO at the WL. A plate-form mold cavity of 125 × 125 mm with two thicknesses (1.5 and 3.0 mm) and two insert shapes (slit with 1 mm width and cylindrical with 15 mm radius) was used, as shown in Fig. 1.

The injection molding was carried out in a DK-Codim 175/410 injection molding machine. The process parameters were fixed as follows: Packing pressure of 40 MPa, injection time of 2.3 s, mold temperature of 60 °C and melt temperature of 250 °C. Plates without insert (i.e. without WL) were injected in order to extract tensile test specimens without a WL at a distance of 25.5 mm after the insert tip. The aim of using the same injection time for both thicknesses was to obtain similar velocities at the flow front, as usually encountered in industrial parts. Using water jetting, tensile test specimens were cut from the plates with WL at six different flow distances from the insert tip: 3.5, 14.5, 25.5, 47.5, 69.5 and 91.5 mm. The flowing WL plane was in the middle of each tensile test specimen, which had a width of 5 mm at this location. The total length of the specimen was 85 mm (Fig. 1).

2.2. Mechanical testing and digital image correlation

Quasi-static tensile tests were carried out using an Instron 5966 machine with an optical extensometer, with a gauge length varied between 10 and 13 mm. The clamp speed was fixed to 10 mm/min. The strain fields under tensile loading of some selected specimens were also evaluated with DIC using a Q-400 system from LIMESS combined with ISTRA4D (4.4.4) software from Dantec Dynamics. In this case, the tensile testing machine was a Schenck POZ 160. The strain fields were analyzed using a pixel size ranging between 17 and 21 μm.

2.3. Thickness measurements

Thickness measurements were made by means of a 3D profilometry technique using a Veeco Dektak 150 with a 12 μm stylus.

2.4. X-ray computed tomography

Some tensile test specimens, cut at flow distances of 3.5, 25.5 and 69.5 mm after the insert, were selected for microstructural analysis and were labelled as positions 1, 2 and 3, respectively, (see Fig. 1). The CT scan was performed directly on the tensile test bar by fixing it on a holder. Volumes of $5 \times 10 \times 3\,mm^3$ or $5 \times 10 \times 1.5\,mm^3$ for 8 cases were scanned, as explained in Table 1.

A CT system GE v|tome|x m 300/180 Metrology Edition with a Nanofocus x-ray tube was employed using the following parameters: Mode 1, x-ray tube voltage 100 kV, x-ray tube current 135 μA, exposure time per projection 500 ms, 3300 projections, no pre-filtration and a voxel size of 2.9 μm. The system used a 16 MPixel detector dynamic 41/100 without any binning. Each scan took ~3 h and resulted in a data set of about 20 GB size.

2.5. Determination of fiber orientation and volume fraction

The CT data were analyzed using VG Studio Max 3.1 software from Volume Graphics. The evaluation of FO and VF was based on a local filtering method, which uses gradient threshold values and computes a local FO for each voxel. This method does not perform a segmentation of single fibers. A regular hexahedral mesh was used for averaging the computed voxel values inside each mesh element. The element size was fixed at 0.2 mm, which is statistically representative for the given fiber content. In fact, it was estimated that on average nearly 70 fibers lie inside each mesh element. The mesh for microstructure reconstruction was placed in such a way that the three main FO tensor components correspond to the directions of the Cartesian coordinates shown in Fig. 1. This means that the a_{11} component corresponds to the FO in x direction (flow direction), a_{22} is the FO in y direction (transversal to flow) and a_{33} is the FO in z direction (thickness direction). These three directions are very close to the main principle directions given the very low values of the off-diagonal tensor components. In the evaluation, the outer layers in flow direction were not considered, i.e. at the water jet boundaries. For each mesh element, VG Studio Max 3.1 computed a second-order FO tensors, as defined by Advani and Tucker [18]. Fig. 2 shows an example of the results obtained on the mesh. The regular

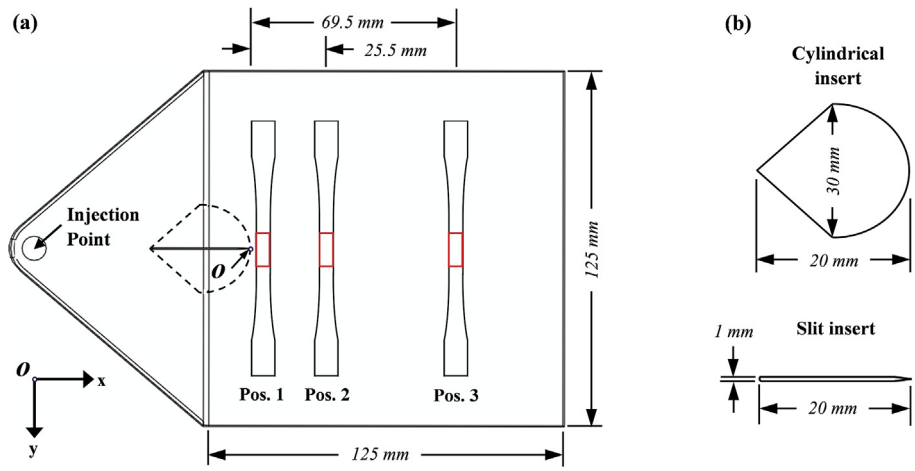

Fig. 1. a-) Plate dimensions of the flowing WL mold cavity. The positions of the X-ray computed tomography scans are marked in red. b-) Dimensions of the inserts used in our study for inducing a flowing WL.

Table 1
Positions of the computed tomography scans for each case of flowing WL.

Flowing WL Case	3.0 mm plate - Slit insert	1.5 mm plate - Slit insert	3.0 mm plate - Cylindrical insert	1.5 mm plate - Cylindrical insert
Positions of CT scans	1, 2, 3	1	1, 3	1, 3

mesh can be divided along a given direction into layers containing the elements at the given direction coordinate. In the following, the FO results are presented by averaging the values of each layer according to the direction of analysis. The standard deviation of the mean value depends on the number of layers under consideration, however their maximal values was of 0.022 for a single evaluation point.

3. Results and discussion

3.1. Mechanical properties of flowing weld lines

Based on previous rheological tests, it was known that the healing ability of the PBT matrix is very high. Indeed, at the selected injection temperature the relaxation time of the unreinforced PBT matrix is approximately 4 ms [9].

This means that the FO is the dominant factor controlling the mechanical properties of the flowing WLs for the material at hand. In fact, V-notches did not appear at the WLs and failure always took place at the WL. In general, a strength reduction factor of 0.85 (reduction of 15%) was found for flowing WLs, which is higher than the factor of frontal WLs [9]. In Fig. 3, the evolution of the mean failure strain and stress along the flowing WL is plotted for all the cases of the experimental work. Breaking of the specimens with WL always took place exactly at the WL plane. Results show that mostly, a slow increase of failure strength and a failure strain towards the values without WL takes place along the distance of the flowing WL. Given the high healing ability of the PBT matrix, the increase of failure strain can be attributed to the changes in FO along the WL. However, while the measured failure stress reflects the WL strength, the measured engineering failure strains do not reflect necessarily the strain levels at the WL.

The measured failure strain with the optical extensometer is in fact the sum of both failure strain at the WL and strain outside of the WL region (Fig. 3). Using DIC during the tensile tests, a local failure strain at the WL of around 4–8% was determined. This means that the increase of engineering failure strain towards the failure strain values of without WL observed in Fig. 3b is related to the changes of FO at and around the WL. Failure stress just after the cylindrical insert for the 1.5 mm plate was the highest compared to other positions along the flowing WL; it even surpassed the quasi-static strength of the case without WL.

These results show the severity of the WLs and the necessity to study the influence of the process-induced microstructure on the mechanical properties at the WL. No V-notches at the WL were found in the samples

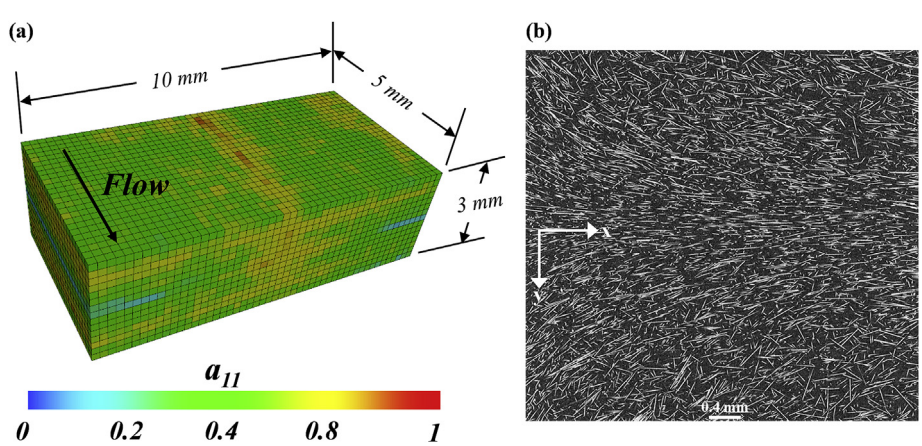

Fig. 2. a-) Visualization of the FO analysis (component a_{11}) in a scanned region via X-ray computed tomography. b-) CT-based image of a section at core (z = 1.5 mm) that shows typical fiber shape and fiber-fiber distance.

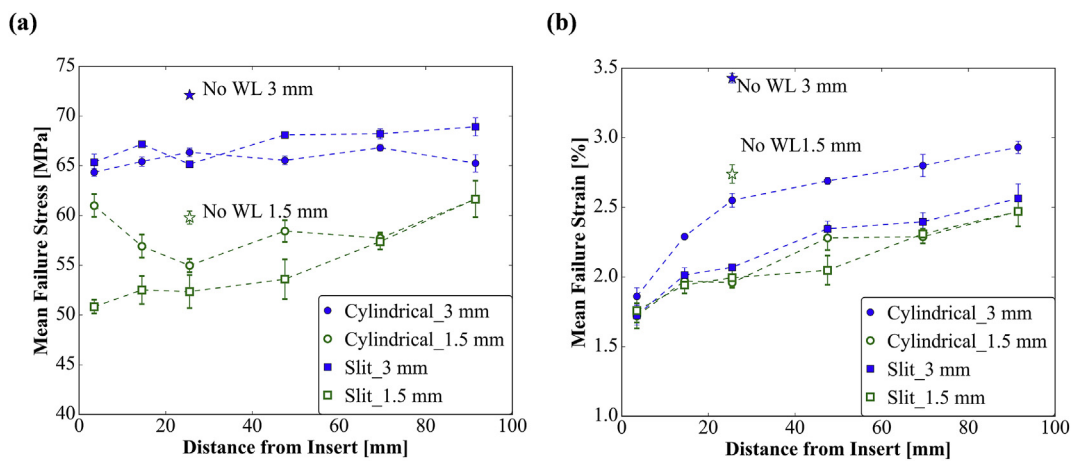

Fig. 3. Evolution of the tensile mechanical properties of the WL along the flow direction (x) for plates with different insert shapes (cylindrical and slit) and different thicknesses (1.5 mm and 3 mm). a-) Engineering failure stress and b-) engineering failure strain.

studied, a fact that rules out their role on the mechanical properties obtained.

3.2. Fiber orientation

In general, the FO of the flowing WLs exhibits some common aspects. The near the WL plane the more the fibers orient in flow direction reaching a maximum of alignment at the WL plane. The FO tensor at the WL plane was similar in all cases, and the tensor component in flow direction (a_{11}) had an average value of 0.8 across the thickness (Fig. 4a). A slight increase of the FO tensor component was also observed in the thickness direction (a_{33}) at the WL. This FO gradient in y direction, transversally to flow direction, can explain the phenomenon of strain localization at the WL observed with DIC. This strain localization could be explained by a higher orientation in the x direction that is perpendicular to the loading direction (y). The width of the FO gradient reached ~8 mm, i.e. ~4 mm from each side of the WL plane. However, the width of the FO gradient varied depending on the part thickness and the flow distance after the insert.

3.2.1. Fiber orientation across the thickness

Fig. 5 presents the FO tensors divided in different layers across the thickness for the 3.0 mm and 1.5 mm plates in order to better understand the induced FO at the WL. Seven layers across the thickness can be identified: Skin, shell, intermediate, core, intermediate, shell and skin. Table 2 shows the thicknesses of the mentioned layers. The skin layer, which is in contact with the mold wall, was the least influenced by the WL, whose FO gradient had a width of ~2 mm (Fig. 5a). The nearer to the core, the greater the FO gradient around the WL. In fact, the FO gradient widened for the shell and inner layers (Fig. 5(b and c)). The width of FO gradient was the largest at the core and reached more than 8 mm in the plate with a thickness of 3 mm. The core layer was highly oriented in the flow direction and showed a slight tendency to orient in the out-of-plane direction, which reached a maximum exactly at the WL plane (Fig. 5d).

Thickness measurements at the WL on the same samples scanned by CT are presented in Fig. 6. An increase of thickness was found at the WL of around 9 µm and 15 µm for the 1.5 mm and 3.0 mm plate, respectively. In the thicker plate, the region of increased thickness was wider. This region of increased thickness was persistent along the WL until the end of the plate.

The increase of FO in the out-of-plane direction at core can explain the changes in plate thickness at the WL presented in Fig. 6. The fact of having more fibers oriented in the thickness direction reduced the shrinkage at the WL in comparison with regions far apart from the WL plane. The typical skin-core microstructure induced by flow between

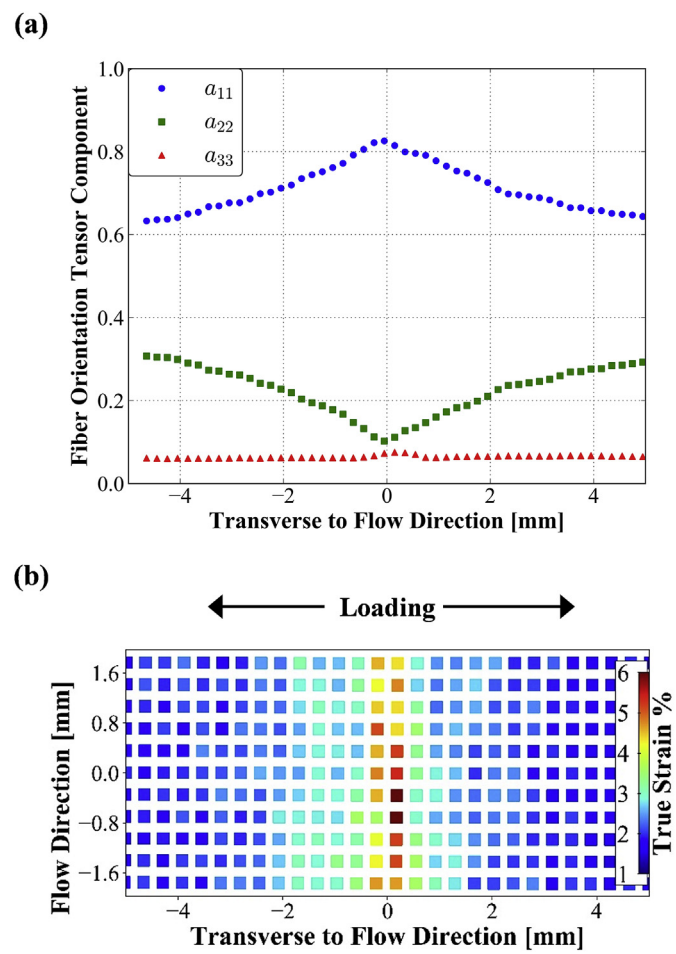

Fig. 4. a-) FO averaged over thickness and flow direction for a flowing WL induced by a slit insert at position 2 (WL at 0 mm). b-) Strain field in loading direction (y) measured with DIC just before failure of the same specimen loaded transversally to the WL.

parallel walls disappeared progressively as the WL plane was approached, where fibers in the core layer were predominately oriented in the flow direction. This shows the huge influence of the WL on the FO, especially in the inner layers of the plate. The later solidification of the inner layers in comparison to the skin layer can explain the higher influence of the flowing WL on the fiber orientation at the core. In the

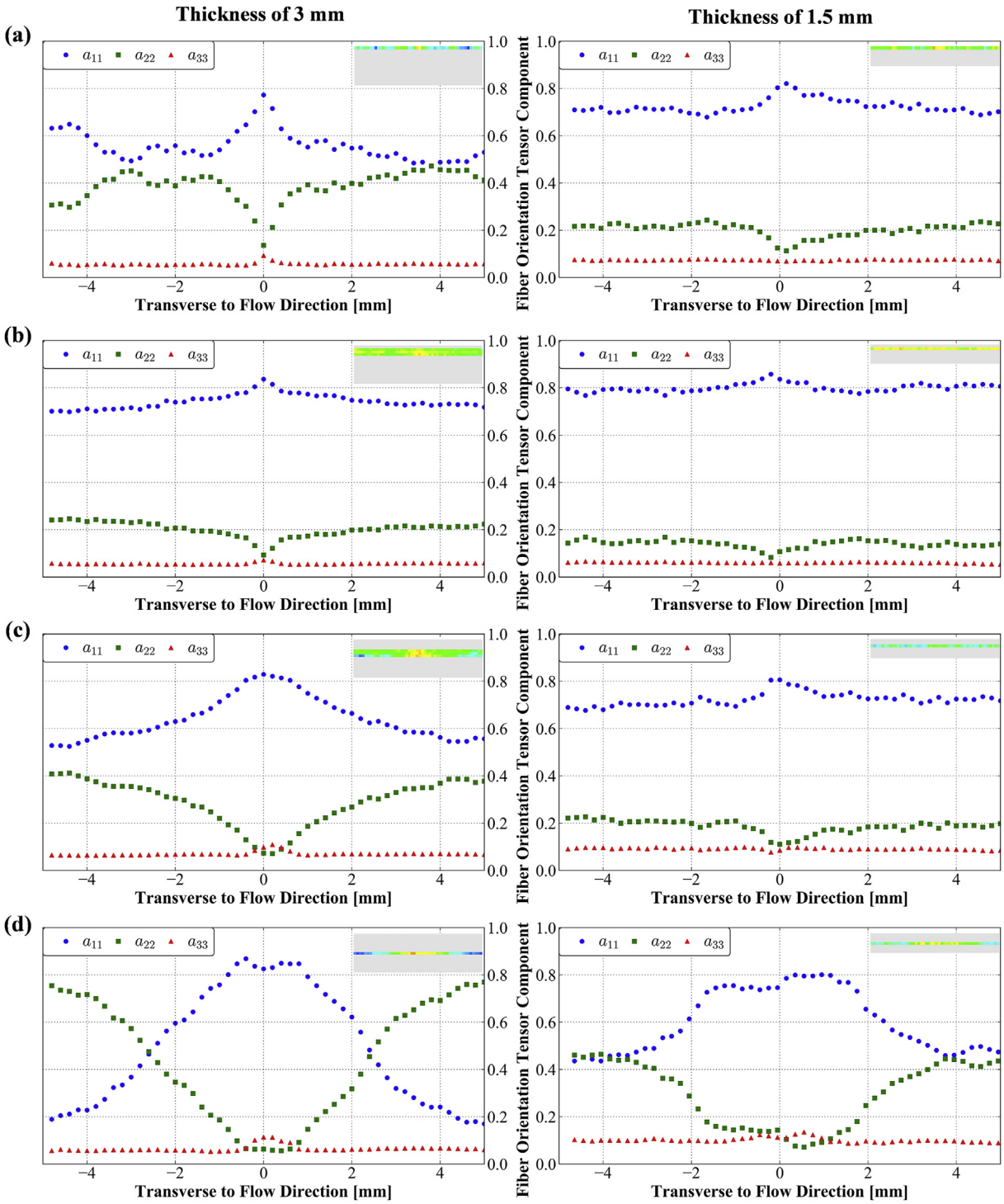

Fig. 5. FO gradient around the WL in the 4 characteristic layers across the thickness for a plate with slit insert at position 1 (3 mm to the left and 1.5 mm to the right): a-) Skin layer, b-) shell layer, c-) intermediate layer and d-) core layer.

Table 2
Thicknesses in z-direction of the identified FO layers at the WL zone.

	Skin	Shell	Intermediate	Core
3.0 mm plate	0.2 mm	0.6 mm	0.6 mm	0.2 mm
1.5 mm plate	0.215 mm	0.215 mm	0.215 mm	0.215 mm

plates of 1.5 mm, the WL had a high influence on the FO only at the core layer, where the width of the FO gradient was ~6 mm. In the other layers, the width of FO gradient was reduced to 2 mm.

Fig. 7 compares the width of averaged FO in thickness direction between the two thicknesses under study. The WL in the thicker plate, which has larger shell and core regions, exhibited a larger FO variation in transversal direction than that of the thinner plate. The difference in FO variation in transversal direction can be explained in fact by the results in Fig. 5. The FO in the thicker plate was more influenced by the weld line compared to the FO in the thinner one. The higher FO in the

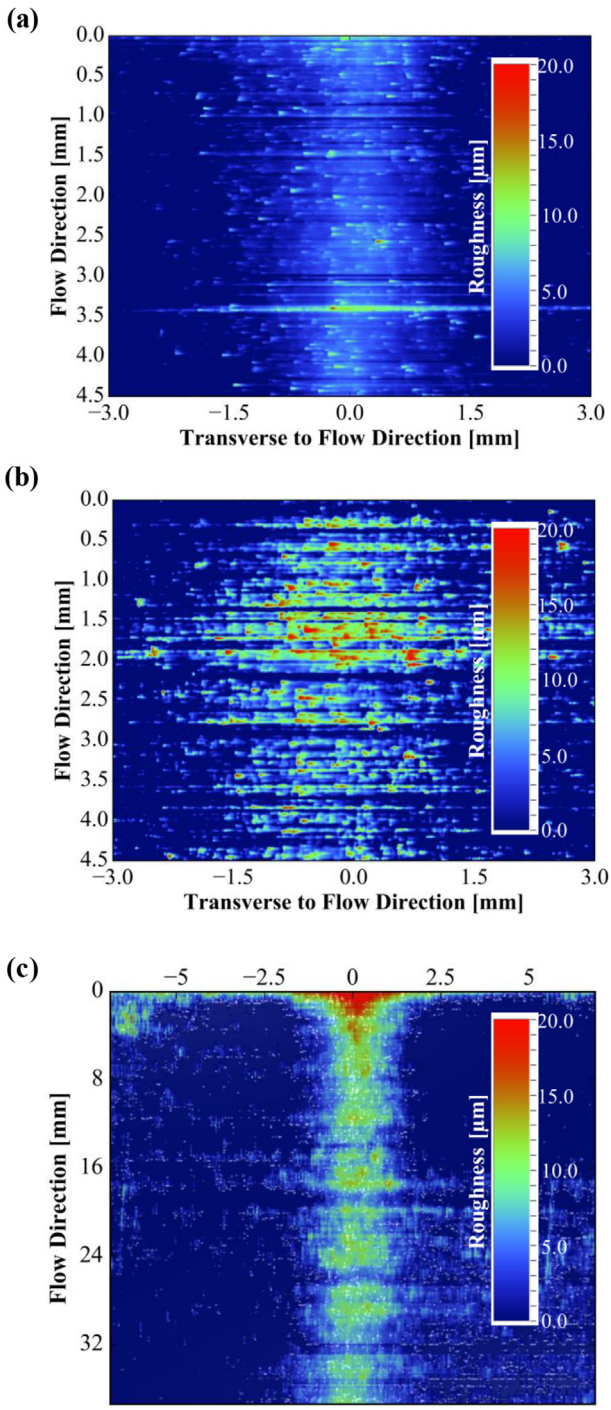

Fig. 6. Thickness variations at the WL area induced in a-) a 1.5 mm plate with slit insert at position 1, b-) a 3 mm plate with a slit insert at position 1 and c-) a 3 mm plate with cylindrical insert.

flow direction across the thickness for the 1.5 mm plate (Fig. 7) explains the lower tensile strength (loading in transversal direction) of the corresponding flowing WLs (Fig. 3).

The preferential FO in the flow direction at the core and the width of FO gradient indicate that a flowing WL has a comparable effect on FO as a mold wall. In fact, similar to a mold wall, the fibers oriented parallel to the WL surface and the FO gradient spread some millimeters from the wall.

In Fig. 8, the averaged FO at the WL across the normalized thickness is compared for the two thicknesses under study. The FO averaging at the WL was performed using all the FO evaluations, which lay at normal

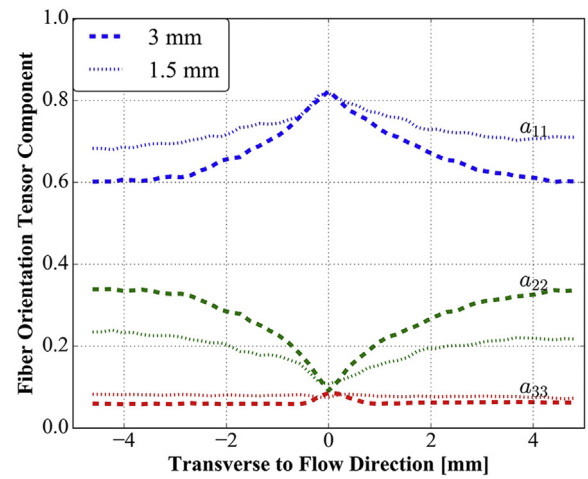

Fig. 7. Influence of the plate thickness on the averaged FO at a flowing WL induced by a slit insert at position 1.

distances shorter than 2 mm from the WL plane (between y = - 2 mm and y = 2 mm). In both slit and cylindrical inserts, the averaged FO profile along the thickness is similar for the two thicknesses under study. The typical core region disappeared with high orientation in the transversal-to-flow direction (y).

3.2.2. *Influence of the insert shape*

To compare the role of the insert shape on the induced FO, Fig. 9 (a and b) compares the slit with the cylindrical insert by averaging, across the thickness, two mesh layers 0.5 mm after the insert and two mesh layers 5 mm after the insert. The induced FO was different at short flow distances (0.5 mm after the insert), but then the induced FO reached a comparable state independently of the insert type. Actually, the FO induced by the cylindrical insert required around 3.5–4 mm after the insert to reach a similar FO state as in the slit insert (Fig. 10). This means that the insert shape has the main influence on the induced FO at the meeting point of the two flow fronts. Simulations of the flow behavior around the cylindrical insert showed that the two flow fronts meet frontally at the beginning of the WL and then the two flows are oriented quickly in the flow direction. The changes in FO just after the insert could be related to the increase of the shearing deformation caused by the insert walls of the cylindrical insert and to the change of the velocity direction of flow front: it is very difficult to quantify the influence of these two phenomena. A slight difference in the FO gradient (variation in transversal direction) was noticed according to the insert used; in fact, the zone of FO distortion around the WL for the slit insert was narrower than that for the cylindrical insert. The insert shape also had an impact on the failure strain along the WL length, as presented in Fig. 3. For example, the specimens extracted from the 3 mm plates with cylindrical insert exhibited a higher failure strain than the specimens extracted from the 3 mm plates with slit insert. This is in agreement with the higher FO gradients in the flowing WLs produced by the slit insert.

In order to get more information about the influence of the insert on the induced FO around the WL, an additional CT scan was performed at position 3 of a 3.0 mm plate injected with a cylindrical insert. The scanned volume was asymmetrical with respect to the WL plane (y = 0) in order to include a larger area transversally to the WL. Fig. 11 shows that the cylindrical insert induced a smaller FO gradient in the transversal direction than the slit insert. As mentioned before, this difference in FO can explain the difference in failure strain presented in Fig. 3, given the fact that a smaller FO gradient in transverse direction would lead to larger failure strains. The microstructural information in Fig. 11 also reveals that the width of the FO gradient can be larger than 10 mm, even after 70 mm of flowing distance.

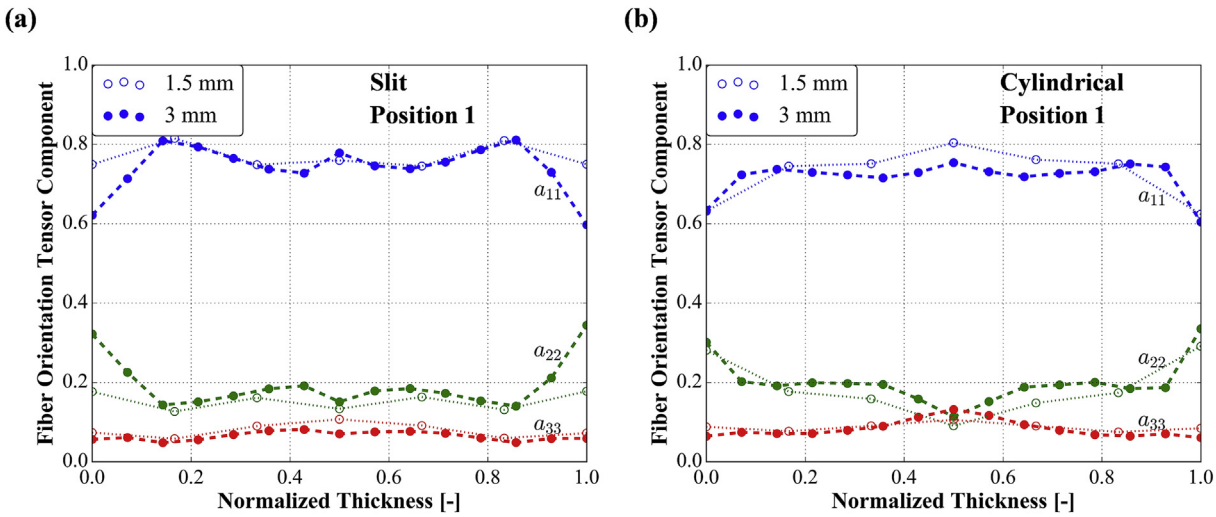

Fig. 8. Averaged FO around the WL region (between y = −2 mm and y = 2 mm) as a function of the normalized thickness at position 1 from a plate with a-) slit insert and b-) cylindrical insert.

Fig. 12 shows the changes of induced FO along the WL for the different insert types. The induced FO tensor at the WL plane and 0.5 mm away from that plane did not change substantially along the WL. However, the FO gradient seems to flatten gradually with the distance from the insert tip. In the 1.5 mm plate, the FO gradient induced by the WL was strongly smoothed after 70 mm.

In order to have a better understanding of the changes along the WL, Fig. 13 presents the induced FO per layers (as in Fig. 5). For the 3 mm plates, the FO gradient changed strongly at short flow distances in the skin and shell layers until it is hardly detectable 65 mm after the insert. The FO gradient in the intermediate layer exhibits, however, progressive decrease with the flow distance. The fibers at core, on the contrary, kept their orientation along the WL with only a slight change 65 mm after the insert tip. In the case of 1.5 mm, after 65 mm of flow distance, the FO gradient is only detectable at skin and core. Unlike at the core, where there was no reorientation along the WL; at the skin, shell and intermediate layers the induced FO at the WL evolved substantially with the flow distance. The existence of a FO gradient along the WL explains why failure always took place at the WL, even when the WL failure stress (90 mm after the insert tip) is comparable to the failure stress of a sample without WL.

The smaller FO gradient for the 1.5 mm plates could explain the quicker increase of the failure stress towards the value of the bulk strength after the insert (Fig. 3), where it can be postulated that the FO

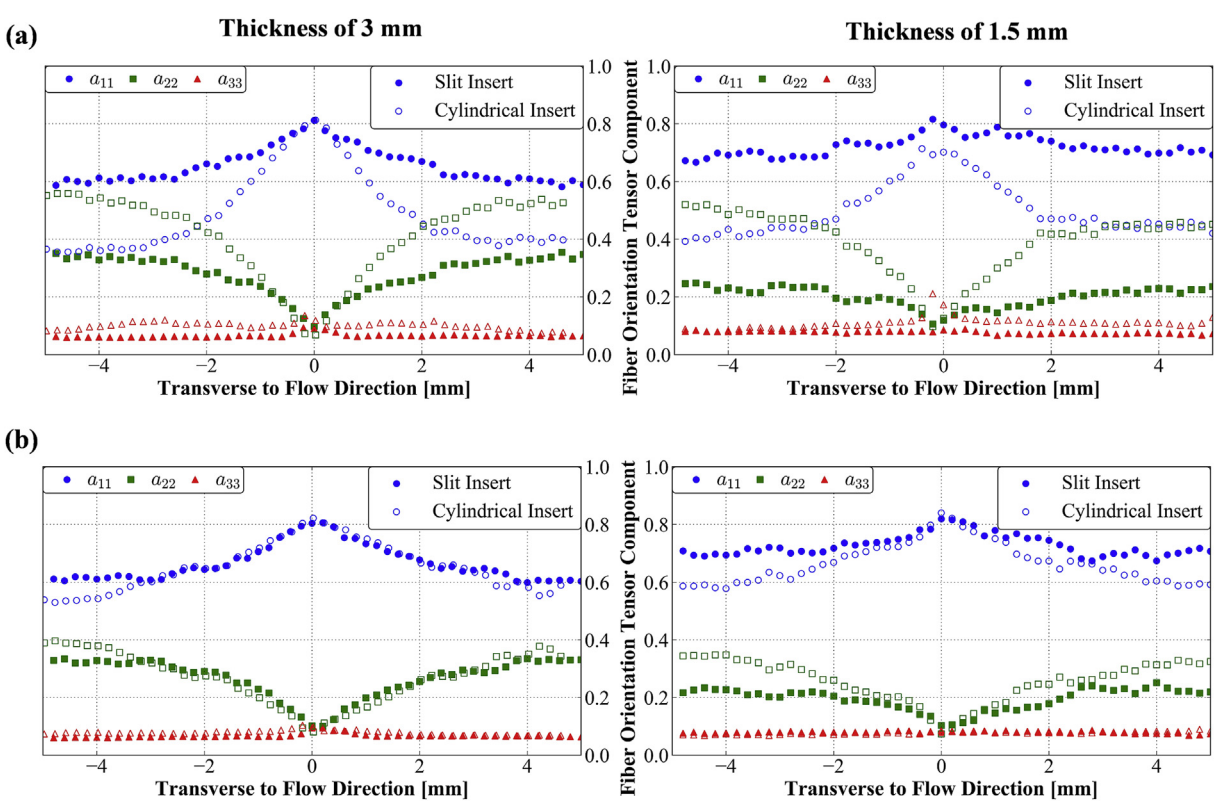

Fig. 9. FO gradient around the WL at different distances from the insert tip (a- 0.5 mm and b- 5 mm) for plates (3 mm on the left and 1.5 mm on the right) with slit and cylindrical insert.

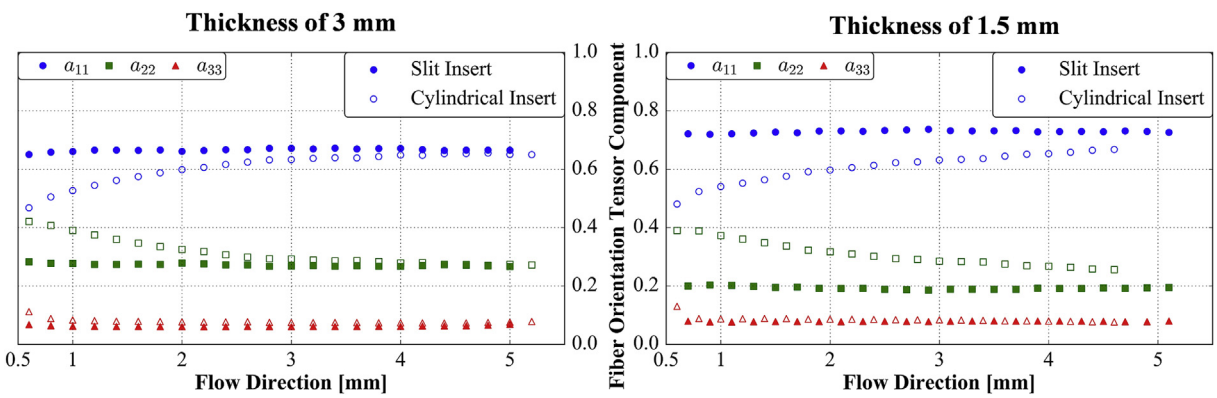

Fig. 10. Evolution of the mean FO along the flow direction for plates (3 mm on the left and 1.5 mm on the right) with slit and cylindrical insert.

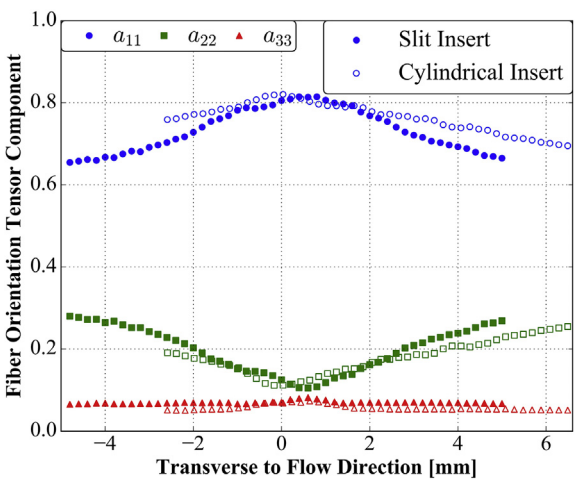

Fig. 11. FO gradient at 65 mm after the insert tip for 3 mm plates with slit and cylindrical insert.

gradient disappeared at shorter flow distances from the insert tip (compared to that one in 3 mm plates), thus, progressively minimizing the WL localization influence. Because of the higher FO in the flow direction obtained in the thinner parts, the FO variation in transversal direction caused by the WL became smaller, which in turn shortened the flow distance for recovering the bulk material strength along the WL.

The part thickness influenced the FO profile along the flow direction. In the 1.5 mm plate, the FO gradient transverse to flow direction across the layers (Fig. 13) was more affected by the flow distance along the WL than that in the 3 mm plate. The similar injection time of both plates induced a higher shear rate in the thinner plate. On one hand, the higher shear rates oriented the fibers predominantly in the flow direction around the WL, reducing the FO gradient at the WL region and enabling a higher increase of the mechanical properties (failure stress and failure strain) towards the values without weld line for the 1.5 mm plates. On the other hand, in the 3 mm plate, only the two outer layers (skin and shell) were influenced by the proximity to the cavity walls and show a reduction of the FO gradient. The lower influence on the intermediate and core layers preserved, in turn, the FO gradient for the 3 mm plate and explains the low increase of mechanical properties along the flow distance.

Using scanning electronic microscopy on the same samples, an FO gradient was found at the core layer, even 91 mm after the insert [9]. The decrease of the FO gradient (transversal to the WL plane) in combination with the strain increase observed in Fig. 3 suggests that the impact of a flowing WL on the mechanical properties would vanish only when the induced FO gradient disappears completely.

3.3. Correlation with DIC results

In order to achieve a better understanding of the mechanical behavior at the WL, the strain field during a quasi-static tensile test of the

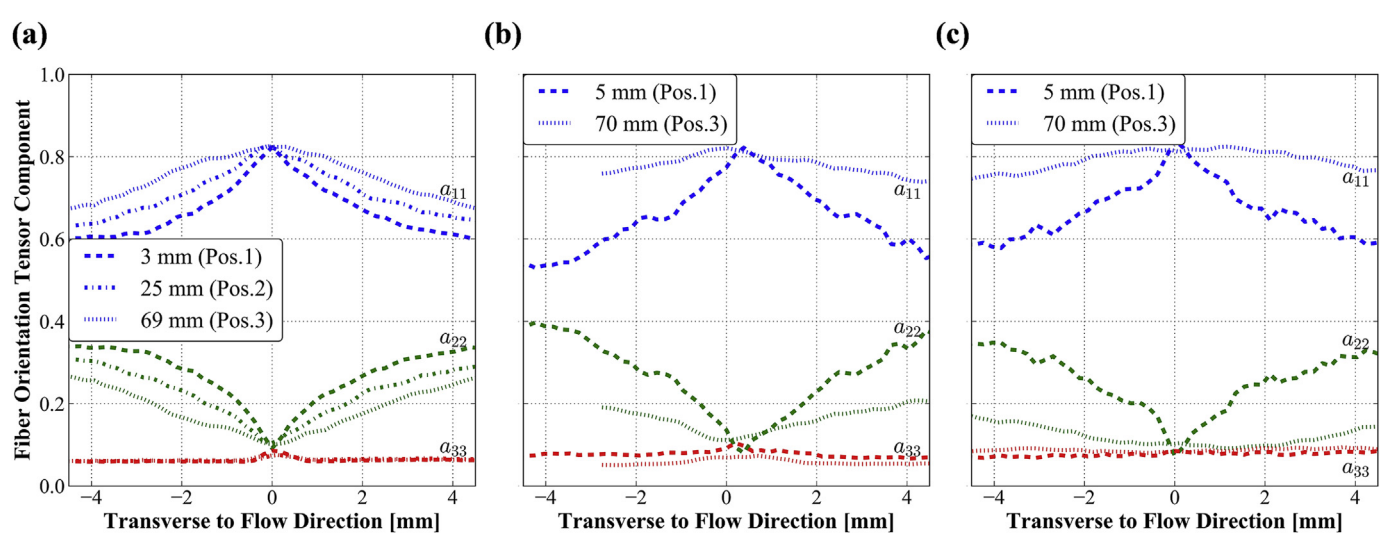

Fig. 12. FO gradient around the WL at different distances from the insert tip in a-) 3 mm plate with slit insert, b-) 3 mm plate with cylindrical insert and c-) 1.5 mm plate with cylindrical insert.

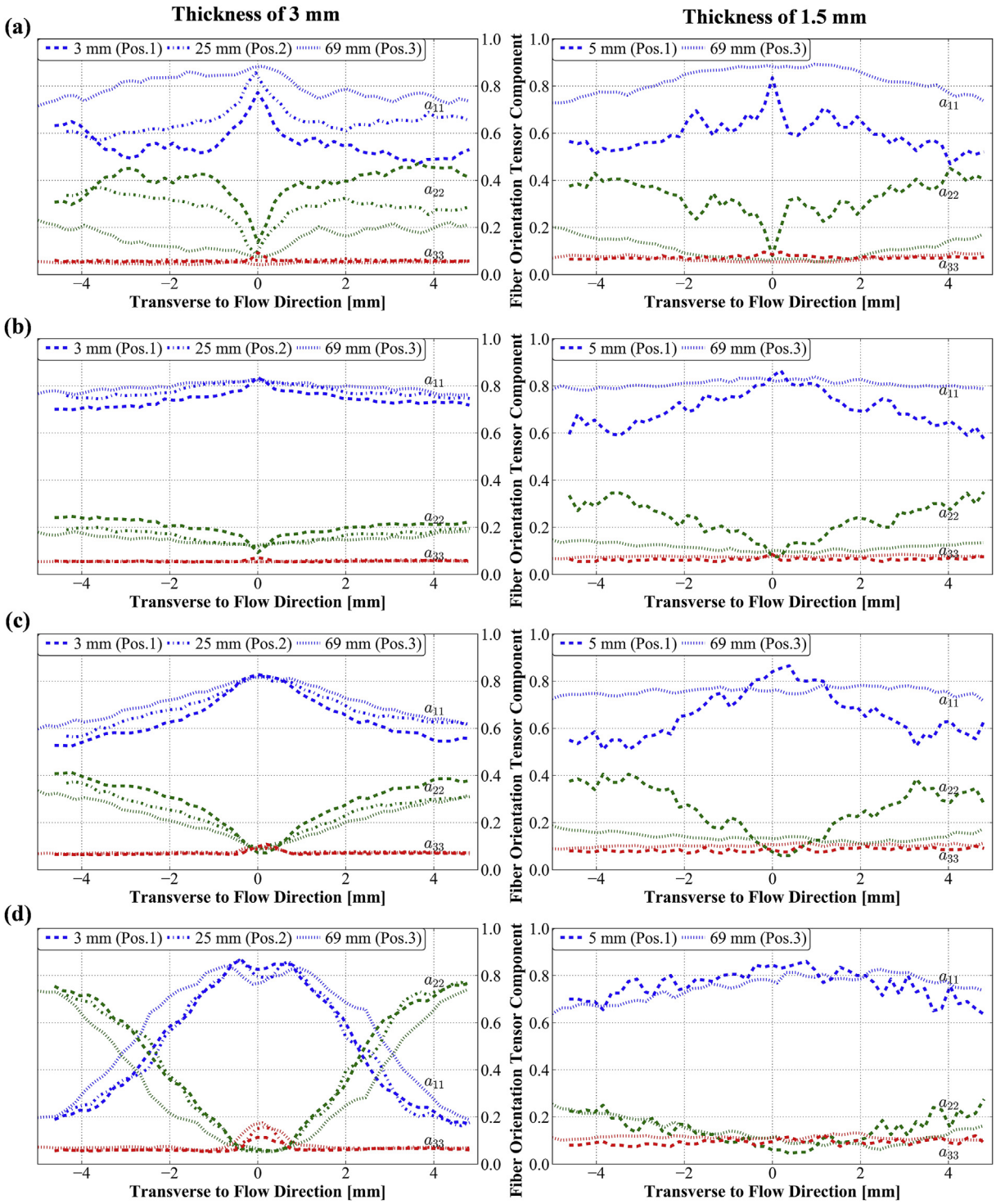

Fig. 13. FO around the WL at different distances from the insert tip in the 4 characteristic layers across the thickness for 3 mm plates with slit insert (left) and 1.5 mm plates with cylindrical insert (right): a-) Skin layer, b-) shell layer, c-) intermediate layer and d-) core layer.

same specimens used for the CT scans was tracked using DIC. In Fig. 14, the strain field in the loading direction (transversal to the WL on one line) is presented for different positions along the WL and for different types of insert. Each strain profile represents the same macroscopic stress level (approximately 60 MPa). A strain gradient, which reaches a width of around 8 mm and has a maximum at the WL plane can be noted. At a given stress level, there was a reduction of the strain gradient with the flow distance from the insert tip. The strain localization at the WL can be correlated directly with the FO gradient shown in Figs. 5 and 13a. The strong strain localization at the WL is, in fact, the result of the unfavorable fiber orientation around the WL (fibers are mainly oriented in flow direction, transversally to the loading direction); which in turn concentrates the stresses in the polymer matrix. The difference in engineering failure strain (measured with extensometer) of the 3 mm samples extracted in position 3 between the slit and cylindrical inserts (Fig. 3b) can be explained in the light of the DIC results in Fig. 14b, where higher strain levels are observed for the cylindrical insert, both at the WL plane and far from it. The strain profiles in

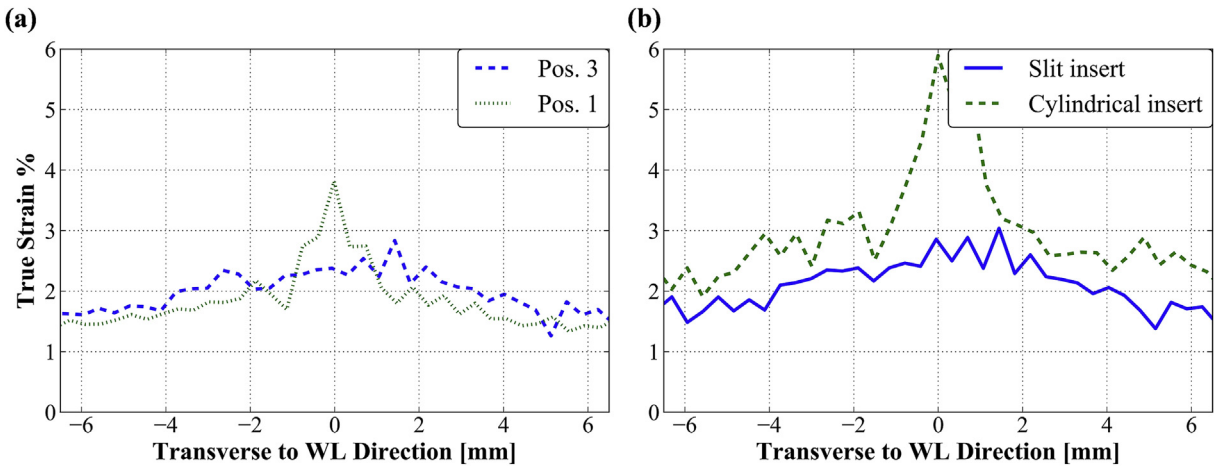

Fig. 14. True strain profile (WL at 0 mm) measured by DIC at a global stress of 60 MPa a-) for 2 positions in the 3 mm plate with slit insert and b-) for specimens in position 3 from 3 mm plates with different inserts.

Fig. 14b correspond to a stress level of ~60.5 MPa, which is close to the failure stress of the sample extracted from the plate with cylindrical insert. The difference of measured strains between the cylindrical and slit insert correlates with the results of FO in Fig. 11. In fact, in the plates with a cylindrical insert the fibers away from the WL plane (2–3 mm from plane) were more oriented in the flow direction than their counterparts in the plates with a slit insert. This would lead to higher deformations when the sample was loaded transversally to the flow direction.

The results from DIC were also used to estimate the local Young's modulus (E) at the WL region and at zones far away from the WL plane. The moduli were calculated by taking the difference of global stress corresponding to a change of local strain going from 0.15% to 0.8%. It was found that the local Young's modulus diminishes with proximity to the WL plane. For all flowing WL cases, E at the WL ranged between 3650 and 3900 MPa. For points in a section 4 mm away from the WL plane, E increased and ranged between 4500 and 5000 MPa. In order to check if the measured local Young's moduli are plausible, the local Young's moduli were estimated analytically by mean field homogenization using the FO measured via CT. The Mori-Tanaka model [20] was chosen for the calculations. In terms of the polymer matrix, a Young's modulus of 2230 MPa and a Poisson's ratio of 0.4 were used. These values were obtained from tensile tests performed on injection-molded samples of the non-reinforced PBT compound. For the E-glass fibers, a Young's modulus of 72 GPa, a Poisson's ratio of 0.22 [21] and an aspect ratio of 20 were set. The analytical calculations were done in two regions, one exactly at the WL plane and the other 4 mm away from the WL plane for the case of 3 mm plate at position 1 with a slit insert. A multilayer representative volume element was generated using the same layers and the FO tensors given in Fig. 13. The glass fiber volumetric fraction was defined equal to 0.18 in all layers. In this framework, estimated theoretical E values at the WL and 4 mm away from the WL plane were equal to 3600 MPa and 4500 MPa, respectively. In front of those theoretical values, the E values determined experimentally via DIC at the WL and 4 mm away from the WL plane were approximately 3730 MPa and 4400 MPa, respectively. These results indicate that, for the material used in this study, the decrease of the Young's modulus in the direction of the WL is related to the FO gradients presented in the Fig. 13.

3.4. Volume fraction

The changes in VF at the flowing WL were very similar, independently of the insert type, position and thickness. To eliminate the uncertainty of the VF analysis at the boundaries of the scan, only a region of 8 mm was considered. Results in Fig. 15 show that, in the shell layer and more notably in the core layer, the VF decreased as the WL plane was approached. One would expect an increase of VF at the core layer in the vicinity of the WL plane due to the higher FO in flow direction, which would facilitate the fiber compaction. This decrease in VF can be explained by the change in flow front velocity at the WL interface. As mentioned in Sec. 3.2, a WL acts as a wall, especially at the core layer. In fact, lower VFs near the cavity walls have been reported in the literature, where the phenomenon was related to high shear rates and fiber migration [22,23]. The same behavior can explain the decrease of fiber content at the WL surface.

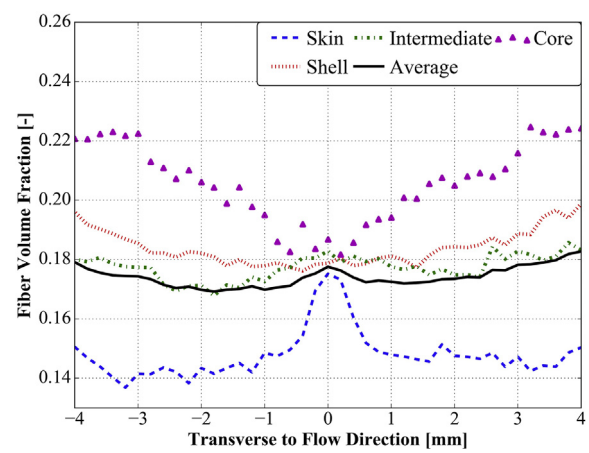

Fig. 15. Fiber volume fraction in a flowing WL induced by a slit insert in a 3 mm plate at position 1. Profiles of fiber VF are given for 4 characteristic layers across the thickness and as average through the whole thickness.

4. Conclusions

A flowing WL acted similar to a mold wall in terms of the induced FO. The largest influence on FO was located at the core layer of the WL in the injection-molded part. A flowing WL induced a large FO variation in transversal direction that reached a maximum at the WL plane. The width of the FO gradient (variation in transversal direction) induced by a flowing WL can be larger than 8–10 mm. The FO gradient slowly decreased along the flow distance, which explains the increase of failure strain and failure stress along the WL. At the flowing WL, there was an increase of fibers oriented in the thickness direction, which modified the shrinkage behavior at the WL and can lead to an increase of the part thickness at the WL.

The insert shape did not influence the local FO at the WL, but had an impact on the FO gradient transversally to the WL plane. A cylindrical insert (diameter of 30 mm) induced a larger FO gradient than a slit insert (width of 1 mm). The flowing WLs in thinner parts exhibited shorter flow distances for vanishing the FO gradient induced by the WL. The induced FO gradient at the intermediate and shell layers disappeared with the flow distance, but the FO gradients at core and skin layers were persistent, even after 90 mm of flow distance.

Local strain analysis assisted by DIC during a quasi-static tensile test proved that the FO gradient at the flowing WL was responsible for the strong strain localization in the vicinities of the WL plane, which led finally to the failure of the specimen.

References

[1] S. Fellahi, A. Meddad, B. Fisa, B.D. Favis, Weldlines in injection-moulded parts: a review, Adv. Polym. Technol. 14 (3) (1995) 169–195 https://doi.org/10.1002/adv.1995.060140302.

[2] R.M. Criens, H.G. Moslé, The influence of knit-lines on the tensile properties of injection molded parts, Polym. Eng. Sci. 23 (10) (1983) 591–596 https://doi.org/10.1002/pen.760231011.

[3] T. Nguyen-Chung, G. Mennig, M. Boyanova, S. Fakirov, F.J. Baltá Calleja, Effect of an obstacle during processing on the weld line of injection-molded glassy polystyrene: microhardness study, J. Appl. Polym. Sci. 92 (5) (2004) 3362–3367 https://doi.org/10.1002/app.20335.

[4] R. Seldén, Effect of processing on weld line strength in five thermoplastics, Polym. Eng. Sci. 37 (1) (1997) 205–218 https://doi.org/10.1002/pen.11663.

[5] G.H. Oh, J.H. Jeong, S.H. Park, H.S. Kim, Terahertz time-domain spectroscopy of weld line defects formed during an injection moulding process, Compos. Sci. Technol. 157 (2018) 205–218 https://doi.org/10.1016/j.compscitech.2018.01.030.

[6] K. Yamada, K. Tomari, U.S. Ishiaku, H. Hamada, Evaluation of mechanical properties of adjacent flow weldline, Polym. Eng. Sci. 45 (8) (2005) 1180–1186 https://doi.org/10.1002/pen.20385.

[7] S.C. Malguarnera, A. Manisali, The effects of processing parameters on the tensile properties of weld lines in injection molded thermoplastics, Polym. Eng. Sci. 21 (10) (1981) 586–593 https://doi.org/10.1002/pen.760211004.

[8] S. Hashemi, Thermal effects on weld and unweld tensile properties of injection moulded short glass fibre reinforced abs composites, Express, Polym. Lett. 1 (10) (2007) 688–697, https://doi.org/10.3144/expresspolymlett.2007.94.

[9] M.B. Baradi, C. Cruz, G. Régnier, Mechanical characterization of frontal and flowing weld lines in injection-molded short fiber-reinforced thermoplastics, Proceedings of the Europe Africa Conference 2017 of the Polymer Processing Society (PPS), Dresden, June, 2017.

[10] S.-J. Liu, J.-Y. Wu, J.-H. Chang, S.-W. Hung, Experimental matrix design to optimize the weldline strength in injection molded parts, Polym. Eng. Sci. 40 (5) (2000) 1256–1262 https://doi.org/10.1002/pen.11253.

[11] J.K. Kim, J.H. Song, S.T. Chung, T.H. Kwon, Morphology and mechanical properties of injection molded articles with weld-lines, Polym. Eng. Sci. 37 (1) (1997) 228–241 https://doi.org/10.1002/pen.11665.

[12] A. Vaxman, M. Narkis, A. Siegmann, S. Kenig, Weld-line characteristics in short fiber reinforced thermoplastics, Polym. Compos. 12 (3) (1991) 161–168 https://doi.org/10.1002/pc.750120305.

[13] F. Prade, F. Schaff, S. Senck, P. Meyer, J. Mohr, J. Kastner, F. Pfeiffer, Nondestructive characterization of fiber orientation in short fiber reinforced polymer composites with X-ray vector radiography, NDT Int. 86 (1) (2017) 65–72 https://doi.org/10.1016/j.ndteint.2016.11.013.

[14] T. Thi, M. Morioka, A. Yokoyama, S. Hamanaka, K. Yamashita, C. Nonomura, Measurement of fiber orientation distribution in injection-molded short-glass-fiber composites using X-ray computed tomography, Mater. Process. Tech. 219 (1) (2015) 1–9 https://doi.org/10.1016/j.jmatprotec.2014.11.048.

[15] C. Hannesschläger, V. Revol, B. Plank, D. Salaberger, J. Kastner, Fibre structure characterisation of injection moulded short fibre-reinforced polymers by X-ray scatter dark field tomography, Case Studies in Nondestructive Test. & Eval. 3 (1) (2015) 34–41 https://doi.org/10.1016/j.csndt.2015.04.001.

[16] A. Ayadi, H. Nouri, S. Guessasma, F. Roger, Determination of orthotropic properties of glass fibre reinforced thermoplastics using X-ray tomography and multiscale finite element computation, Compos. Struct. 136 (1) (2016) 635–649 https://doi.org/10.1016/j.compstruct.2015.10.041.

[17] A. Ayadi, H. Nouri, S. Guessasma, F. Roger, Large-scale X-ray microtomography analysis of fiber orientation in weld line of short glass fiber reinforced thermoplastic and related elasticity behavior, Macromol. Mater. Eng. 301 (8) (2016) 907–921 https://doi.org/10.1002/mame.201500463.

[18] S.G. Advani, C.L. Tucker III, The use of tensors to describe and predict fiber orientation in short fiber composites, J. Rheol. 31 (8) (1987) 751–784 https://doi.org/10.1122/1.549945.

[19] J. Kalus, J.K. Jørgensen, Measuring deformation and mechanical properties of weld lines in short fibre reinforced thermoplastics using digital image correlation, Polym. Test. 36 (2014) 44–53 https://doi.org/10.1016/j.polymertesting.2014.03.017.

[20] T. Mori, K. Tanaka, Average stress in the matrix and average elastic energy of materials with misfitting inclusions, Acta Metall. Mater. 21 (1973) 571–574 https://doi.org/10.1016/0001-6160(73)90064-3.

[21] J.-M. Kaiser, M. Stommel, Modified mean-field formulations for the improved simulation of short fiber reinforced thermoplastics, Compos. Sci. Technol. 99 (2014) 75–81 https://doi.org/10.1016/j.compscitech.2014.05.010.

[22] G.M. Vélez-García, P. Wapperom, D.G. Baird, A.O. Aning, V. Kunc, Unambiguous orientation in short fiber composites over small sampling area in a center-gated disk, Composer Part A – Appl Sci 43 (2012) 104–113 https://doi.org/10.1016/j.compositesa.2011.09.024.

[23] H.-C. Tseng, T.-C. Wang, Y.-J. Chang, C.-H. Hsu, R.-Y. Chang, Progress on fiber concentration for injection molding simulation of fiber reinforced thermoplastics, ANTEC Conf. Proc. 2 (2014) 1689–1693.